Quantitative Comparison of Microtexture in Near-Alpha Titanium Measured by Ultrasonic Scattering and Electron Backscatter Diffraction

ADAM L. PILCHAK, JIA LI, and STANISLAV I. ROKHLIN

Ultrasonic backscattering and attenuation data were collected and processed using recently developed theoretical models to estimate the directionally dependent, volume-averaged size, and morphology of microtextured regions (MTRs) in a near-α Ti-8Al-1Mo-1V bar. The sample was also interrogated with electron backscatter diffraction from which MTR sizes were obtained by either manual segmentation and linear intercept analysis or fitting the spatial autocorrelation of similarly oriented c-axes to the geometrical autocorrelation function used in the scattering model. The results of the ultrasonic inversion were in good agreement with the EBSD measurements for the radial direction but were off by a factor of ~2.45 for the longitudinal direction. Reasons for the discrepancy were discussed and strategies to improve the agreement were made.

I. INTRODUCTION

USING current industrial conversion practices, most near-α and α + β titanium alloy mill products contain large regions of primary alpha particles which have similarly oriented [0001] axes of the hexagonal close-packed unit cell. These are commonly known as microtextured regions (MTRs) or macrozones. We adopt the former nomenclature in this manuscript to emphasize that the grains comprising these regions are textured on the microscopic scale but recognize that they may collectively form a larger zone which is evident macroscopically.[1] The detection of these regions has been made possible with the advent of electron back-scatter diffraction (EBSD) technology in which local crystallographic orientation measurements are made in a scanning electron microscope. It is widely accepted that MTRs are deleterious to room temperature dwell fatigue properties,[2–5] but recent fractographic studies suggest that microtexture may also contribute to lifetime variability in conventional fatigue as well.[6]

Significant effort has been made to understand the mechanisms associated with the formation of, or, perhaps more appropriately, the preservation of micro-texture during α + β working. A typical ingot to billet (or bar) conversion route consists of a β homogenization step followed by β working, α + β working, and finally finishing with α + β annealing. MTRs have their origins in the β quench stage following β working prior to α + β processing. In materials with large cross sections, the low thermal conductivity of titanium controls the cooling rate which, in many cases, is slow enough to result in the formation of large α colonies consisting of parallel plates of α phase with the same crystallographic orientation. The orientations of the α lamellae and the retained β phase adhere to Burgers orientation relationship (OR), i.e., $(0001)_\alpha \parallel (110)_\beta$ and $[2\bar{1}\bar{1}0]_\alpha \parallel [1\bar{1}1]_\beta$. During α + β working, the lamellar α colonies are broken down through a process known as spheroidization[7–9] resulting in the formation of equiaxed particles that appear "recrystallized" in the morphological sense, but these particles often maintain similar c-axis orientation. The term spheroidization is used to describe this mechanism to denote that it is distinct from classical discontinuous recrystallization where there is long range migration of high angle boundaries. Spheroidization begins dynamically during deformation but is completed during the α + β annealing stage where the operative mechanisms include subgrain boundary grooving and termination end migration.[10,11] These processes usually require one to several hours to complete depending on the degree of deformation imposed during prior working steps and the annealing temperature. No significant lattice rotations are expected during this stage, but it has been shown that different cooling rates can cause the strength of the resultant *macrotexture* to change.[12] Moreover, if the annealing temperature is chosen to be high in the α + β phase field, with an appropriately fast cooling rate, one can take advantage of the decomposition of the β phase into α + β colonies which insulate the similarly oriented primary α particles from one another by separating them with a multi-variant, basket weave structure, or at minimum, a differently oriented α colony. Occasionally, however, because the β orientation within a given MTR may rotate in a similar direction as the primary α particles (since two of the dominant slip systems are initially aligned) variant

ADAM L. PILCHAK, Materials Research Engineer, is with the Air Force Research Laboratory, Materials and Manufacturing Directorate, AFRL/RXCM, Wright Patterson AFB, OH 45433. Contact e-mail: adam.pilchak.1@us.af.mil JIA LI, Graduate Research Associate, and STANISLAV I. ROKHLIN, Professor, are with Department of Materials Science and Engineering, The Ohio State University, Columbus, OH 43210.
Manuscript submitted July 23, 2013.
Article published online July 3, 2014.

selection during decomposition of β to $\alpha + \beta$ may result in primary α particles and secondary α colonies having similar orientation.[13,14]

The strong plastic anisotropy of the α phase leads to complex strain partitioning among the colonies during processing. As a result, some colonies are spheroidized more readily than others. Colonies with the [0001] axis along the primary working direction (for axisymmetric processes) are difficult to deform, because they require the activation of $\langle c + a \rangle$ slip systems which have higher flow stress than the $\langle a \rangle$ slip systems. The degree of spheroidization is generally much less in these so-called hard-oriented colonies compared to colonies where both basal and prism slip are operative. The latter configuration has been shown to be most effective at randomizing the grain orientations within the prior α colonies.[8] Consequently, the resultant material can be thought of as having a matrix with low microtexture that has a "second phase" of microtextured regions within it when considered on a large length scale.

The presence of MTRs affects sonic inspectability[15] and fatigue properties. There have been few efforts to quantify it objectively and even fewer attempts to correlate it directly with material behavior. A notable exception is the work of Woodfield et al.[2] who were the first to show clearly the existence of microtexture in Ti alloys using EBSD, which was in its infancy, and therefore time consuming, at this time. The authors used a misorientation angle tolerance of 1.25 and 20 deg to define the primary α particles and MTRs, respectively. These tolerances were determined empirically by comparing the results of automated computer analysis and manual inspection of two-dimensional (2D) EBSD maps and micrographs. Using these metrics, the authors were able to obtain a good correlation between MTR size (among other parameters) and dwell fatigue lifetime for Ti-6242 produced under various processing routes using a regression model. Pilchak et al.[6] have shown a qualitative correlation between the degree of microtexture and low cycle fatigue lifetime in Ti-6Al-4V. Samples with large clusters of microtexture that formed large clusters of facets on the fracture surface had lower fatigue lifetime. This was attributed to the reduced resistance to small-faceted crack growth caused by the lack of high angle boundaries within the MTRs. The authors used quantitative tilt fractography to identify the range of c-axis orientations that resulted in the formation of fatigue facets near the crack initiation site and segmented EBSD based on this criteria. Next, line profiles in the direction of crack growth were used to quantify the size of the interconnected regions of facet-forming grains. Minimum fatigue lifetimes for each lot of material were then compared and correlated well with the maximum MTR size measured in the direction of crack growth.

With respect to wave propagation, MTRs essentially behave as large grains with elastic properties averaged over their constituents.[16] As a result, MTRs strongly scatter ultrasonic waves in the MHz frequency range which is the frequency range commonly used for ultrasonic inspection of aerospace components. It is well known that strong ultrasonic scattering is responsible for "sonic noise" during ultrasonic inspection of titanium alloys, and this has been studied extensively.[15,17–19] These investigations reported on the interaction of ultrasonic waves with microstructural features and have discussed microstructurally induced sonic noise in titanium alloys and its consequences on ultrasonic inspection and acceptance of forgings. Scattering-induced ultrasonic attenuation and ultrasonic backscattering are two measurable ultrasonic characteristics that can potentially be utilized to characterize the extent of microtexture in a given material in the production environment. The ultrasonic attenuation coefficient is a characteristic of the total ultrasonic scattering along the propagation path that leads to decay of ultrasonic energy.[20] For its accurate measurement, one needs relatively flat parallel surfaces of the inspected component, and it is an averaged characteristic over the component thickness. The ultrasonic backscattering coefficient, on the other hand, characterizes the energy scattered back to the emitting transducer in between the front and back reflections; it is simpler to measure and potentially offers better spatial resolution of microstructural variability. Most importantly, it can be further processed to obtain quantitative measurement of microstructural features.

The first studies of backscattering in realistic titanium alloy microstructures were presented by Han and Thompson[21] and Panetta et al.[22] Blodgett and Eylon[23] have studied experimental attenuation and backscattering in titanium alloys and paid special attention to material macrotexture. Later, Bhattacharjee et al.[20] demonstrated a quantitative relationship between ultrasonic attenuation and average MTR size in the direction of wave propagation for several near-alpha titanium alloy forgings. The authors obtained reasonable agreement with the attenuation-based model of Yang et al.[24] for titanium alloys with equiaxed MTRs. In fact, MTR shape depends on processing history and, in particular, strain path. For example, initially equiaxed alpha colonies are elongated in the rolling direction and compressed in the thickness direction during hot rolling.[7] Humbert et al.[25] demonstrated that differences in MTR morphology causes variations in ultrasonic backscattering response. The authors investigated two different lots of IMI-834 and found spatial variations in the intensity of MTRs and related these to the backscattered ultrasound signature. The authors calculated the spatial autocorrelation of the component of the elastic stiffness tensor in the direction of wave propagation which revealed the clustering of orientations into MTRs and a periodicity to the bands of microtexture. Recently, ultrasonic wave scattering in forged titanium alloys with nonequiaxed MTRs has been modeled and related to attenuation and backscattering measurements by Yang et al.[16,26] The practically important inverse problem of determining MTR size and geometry from ultrasonic backscattering measurements was addressed by Lobkis and Rokhlin,[27] Lobkis et al.[28] and Li et al.[29]

In this investigation, we expand on prior work in which ultrasonic attenuation[20] data were related to the effective size of MTRs in one direction of wave propagation in near-alpha titanium forgings. Specifically, both ultrasonic attenuation and backscattered

measurements collected in three orthogonal directions were processed in this work to obtain volume-averaged estimate of the size and aspect ratio of highly elongated MTRs in a Ti-8Al-1Mo-1V bar. These sizes were compared with quantitative measurements of MTR size from EBSD data.

II. MATERIALS AND EXPERIMENTAL PROCEDURES

A. *Material*

The material utilized in the present investigation was 152-mm diameter Ti-8Al-1Mo-1V bar supplied by TIMET (Henderson, NV). The as-received material was in the $\alpha + \beta$ worked condition consisting of ~65 pct primary α with the remainder being $\alpha + \beta$ colonies and retained β phase. A 12.54-mm-thick piece of the bar was sectioned perpendicular to the bar axis with wire EDM. Next, a 25.4 mm × 25.4 mm to be used for ultrasonic measurements was cut from this slice. Samples for metallography and EBSD were prepared at similar radial positions relative to the bar center but from different physical locations in the bar. This was deemed acceptable, because an axially symmetric deformation process was used to produce the bar. Thus, all similar radial locations experienced the same strain at the continuum scale.

B. *Characterization, Data Reduction, and Analysis*

The microstructure, texture, and microtexture of the as-received material were investigated by means of scanning electron microscopy and EBSD, respectively. Imaging was performed in a Sirion (FEI, Hillsboro, OR) at an accelerating voltage of 20 kV with a spot size of "5" (the actual probe current was not measured) at a working distance of 5 mm. EBSD data were collected at the same accelerating voltage with a 49 nA probe at a working distance of 25 mm with the sample surface inclined 20 deg relative to the electron beam.

Both low and high resolution EBSD scans were acquired. The former consisted of nine 144.9 μm × 144.9 μm tiles with a 0.3 μm step size from which the phase fractions and β phase texture were calculated. The coarser resolution scans covered large areas of the samples utilizing a combination of standard beam control scans and automated stage movements[30] after which the individual tiles were stitched using open source software.[31] A scan of the longitudinal section of the bar consisted of 702 individual tiles, 460 μm × 460 μm each, at a resolution of 10 μm covering an area of 12.68 mm × 12.21 mm. The scan on the transverse section of the bar, performed at the same resolution, was 28 mm × 16 mm. A subset from the center of this large scan was selected for manual tracing of the MTRs followed by analysis using the line intercept method. This subset measured 14.82 mm × 14.82 mm.

1. *Line intercept method*
Crystal orientation maps were created in which each pixel was assigned a color from the standard triangle depicting the particular {*hkil*} plane that was perpendicular

to a particular direction (the wave propagation direction) in the sample reference frame. Next, the MTRs in the dataset were identified and traced manually by locating clusters of similar color and therefore orientation. Finally, the line intercept method was used to quantify the size of the regions in a particular ultrasonic wave propagation direction. Depending on sectioning plane, intercepts were calculated in the horizontal or vertical directions on the images. The intercept lengths for "random lines" were determined by rotating the image and using a bilinear interpolation scheme to remap the boundaries between MTRs back onto a square grid where vertical and horizontal lines were again used to calculate intercepts.

2. *Spatial autocorrelation*
In the broadest sense, microtexture is defined simply as clustering of α phase with similar c-axis orientation. The particular reference to [0001] is because of the strong dependence on elastic and plastic properties as a function of angle relative to this axis. Autocorrelation is an effective method to quantify the spatial statistics of similar features in a signal (or image) and is used here to quantify spatial clustering of [0001] axes. Quantifying microtexture in this way is also beneficial as it provides a common language between microstructure and ultrasonic scattering theory.[32–34]

An approach for calculating the spatial autocorrelation of similarly oriented c-axes for an arbitrary vector **r** in the microstructure has thus been formulated in this work. A uniform two-dimensional grid with nodal coordinates (X_i, Y_i) is first mapped onto the northern hemisphere of a unit sphere giving each node new coordinates (x_i, y_i, z_i) thereby creating equal-area "bins"[35]:

$$\mathbf{x} = (x_i, y_i, z_i)$$
$$= \left(\sqrt{1 - \frac{X_i^2 + Y_i^2}{4r^2}} X_i, \sqrt{1 - \frac{X_i^2 + Y_i^2}{4r^2}} Y_i, \quad r - \frac{X_i^2 + Y_i^2}{2r} \right),$$
$$[1]$$

where r is the radius of the sphere, and $\mathbf{x}$ is the set vectors of all nodes following projection onto the sphere. The density of the initial grid (X_i, Y_i) defines the effective resolution on the sphere which we define as the angular distance between the nodes on the sphere. The EBSD data were then analyzed to determine a set of unit vectors, $\mathbf{c}$, parallel to [0001] from each of the measured (Bunge) Euler angles with Eq. [2]:

$$c_x = \sin(\varphi_1) \sin(\Phi)$$
$$c_y = -\cos(\varphi_1) \sin(\Phi) \qquad [2]$$
$$c_z = \cos(\Phi)$$

Each pixel was then mapped to its nearest node by minimizing the angle between $\mathbf{c}$ and $\mathbf{x}$:

$$\min(\cos^{-1}(\mathbf{x} \cdot \mathbf{c})) \qquad [3]$$

Binary images (f_i) were then created for each node which consisted of 1's for each pixel in that node and zero elsewhere. The autocorrelation of these images was individually calculated as

$$A_i = \mathcal{F}\{f_i \circ f_i\} = \mathcal{F}\{f_i\} \cdot (\mathcal{F}\{f_i\})^* \qquad [4]$$

where $\mathcal{F}$ denotes the fast Fourier transform (FFT), $\circ$ denotes convolution (not multiplication), $\bullet$ denotes element-by-element multiplication, and the asterisk denotes the complex conjugate. Because the spatial autocorrelation of similarly oriented pixels was of interest (regardless of the *actual* spatial orientation of the c-axes), an average autocorrelation A was obtained by summing all of the individual autocorrelations element by element:

$$A = \sum_i A_i \qquad [5]$$

Once normalized by the number of elements in the system, N, the autocorrelation is equivalent to the two-point correlation of similarly oriented c-axes, $\mathbf{S}_2^c$:

$$\mathbf{S}_2^c(\mathbf{r}) = A/N \qquad [6]$$

Thus, $\mathbf{S}_2^c(\mathbf{r})$ is the probability that the head and tail of $\mathbf{r}$ will have similar c-axis orientation.

C. *Ultrasonic Measurements*

The rectangular sample cut from the Ti-8Al-1Mo-1V bar stock for ultrasonic measurements is shown in Figure 1. The sample is defined in a coordinate system {**r1**, **r2**, **z**} where **r1** and **r2** are two orthogonal radial directions in the bar, and the **z**-axis (axial direction) was parallel to the bar axis. The largest surface of the sample was perpendicular to the **z**. Ultrasonic backscattering and attenuation measurements were conducted by the pulse-echo immersion technique at normal incidence in three orthogonal directions parallel to the six faces of the sample, *i.e.*, in each of the {**r1**, **r2**, **z**} directions. Ultrasonic signals were excited and received by a pulser/receiver (Panametrics, USA) operating in pulse-echo mode. The ultrasonic signals were acquired and digitized, using a 12-bit, 125 MHz digitizing board, for later processing. A 12.7-mm-diameter plane ultrasonic transducer with about 12 MHz central frequency of the received signal spectrum was used in the measurements. The transducer was positioned 20.5 mm from the top surface of the sample and carefully aligned to assure normal incidence of the ultrasonic wave. Data acquisition and data processing were performed using an in-house computer control system. For attenuation measurement, the intensity of the front surface reflection (FR) and the first back wall reflection (BR), Figure 2(a), were acquired, digitized, and stored for attenuation coefficient determination. The transducer beam diffraction correction was accounted for, and the data processing procedure was used as described in Reference 20. The attenuation measurements were performed in two modes from each sample face: (1) In scanning mode,

signals were acquired with a step size of 0.5 mm, from 441 positions on axial faces and from 17 positions on **r1** and **r2** faces; and (2) in manual mode, where signals from 9 positions were collected on the axial faces and from 3 positions on the **r1** and **r2** faces; in this mode, the transducer was aligned manually at each position.

The intensity of the backscattered energy was significantly less than the front or back wall reflections which necessitated significant amplification of the signal as shown in Figure 2(b) which, of course, led to saturation of the front and back reflections (backscattering signal (BS) appears in Figure 2(b) as noise between the saturated front and back reflections). The procedure for the backscattering data collection is similar to that described in detail previously.[28] Backscattering signals were collected in scanning mode at the same locations as the attenuation measurements. Time averaging of the digitized signals was performed at each spatial position of the scan to reduce electronic noise. Then about 1.75 μs of backscattering trace along the **z**-direction of the sample and 5.8 μs along the **r1** and **r2** directions was gated for FFT (these gate times correspond to about 5.5 and 18.3 mm of sample thickness, respectively). Next, spatial averaging was performed to obtain the averaged RMS of the backscattering signal

$$RMS(f) = \sqrt{\frac{1}{N}\sum_{i=1}^{N}|V_i(f)|^2}, \qquad [7]$$

where $V_i(f)$ is the backscattering amplitude as function of frequency, f, at spatial position i, while N is the total number of spatial positions in a given scan. The absolute values of the backscattering signal RMS depend on the measurement system (the transducer and the pulse/receiver) and the material microstructure,[28] and it requires further processing in order to acquire material microstructure information, which will be discussed in detail in the next section.

D. *Relationship Between EBSD and Ultrasound Measurements*

The autocorrelation obtained from EBSD contains the complete set of statistics describing microstructural length scale, morphology, texture, and all spatial correlations; however, the information is convoluted. If one assumes that a particular set of statistics underlies the measured autocorrelation function, it is possible to extract important metrics like the mean linear intercept[33] or the specific surface area (grain boundary area per unit volume).[36] Introducing the same statistical metrics in the ultrasonic scattering model allows one to directly relate the two different characterization methodologies. Our inverse approach for determination of MTR size and morphology is based on scattering models[16,27–29] which utilize the microstructure statistics originally proposed by Stanke and Kino[32] for equiaxed grains. These models relate the measured scattering behavior to the covariance of elastic constants fluctuations, *i.e.*, microstructural length scale. The extension to nonequiaxed grains has been made possible through the
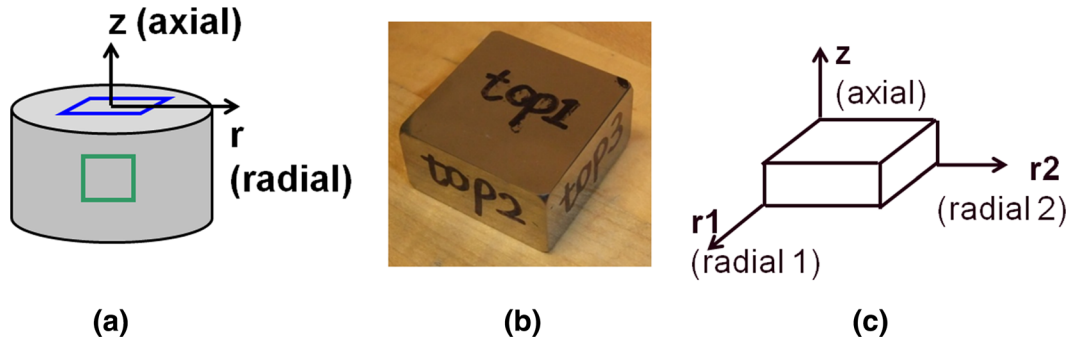
Fig. 1—(a) Coordinate system for the original bar stock and (b, c) the corresponding laboratory coordinate system for the ultrasonic sample.
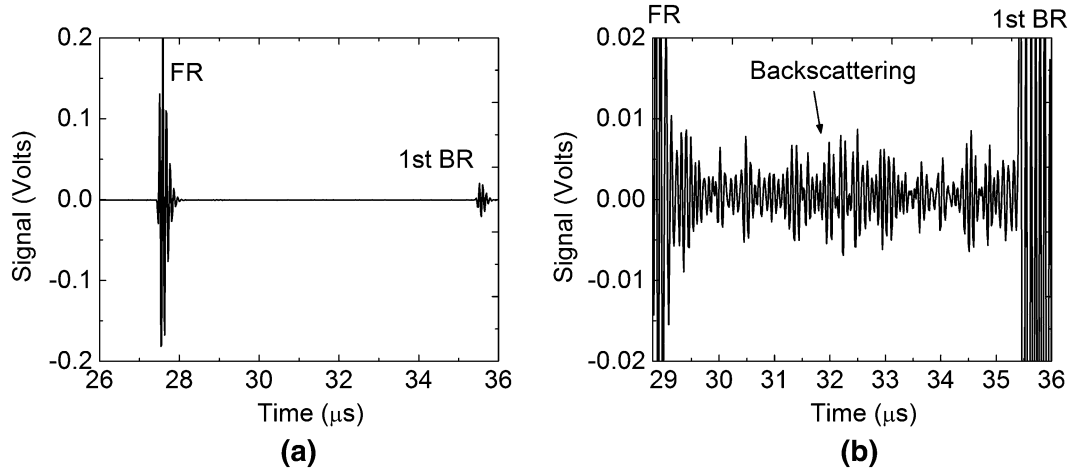

Fig. 2—(a) Typical time-domain signals showing the front surface reflection (FR) from water-sample interface and the first back wall reflection (1st BR) from the back sample-water interface; (b) backscattering signal vs time, where signal in (b) is amplified 126 times relative to that shown in (a) resulting in saturation of the front and back reflections.

generalized Poisson geometrical autocorrelation function[16,21,27–29,37]:

$$w(x, y, z) = \exp\left(-\sqrt{\frac{x^2}{(a_{MTR}^{r1})^2} + \frac{y^2}{(a_{MTR}^{r2})^2} + \frac{z^2}{(a_{MTR}^{z})^2}}\right),$$

[8]

where a_{MTR}^{i} are the correlation lengths (also the mean MTR cord length under the assumption of Poisson statistics[33,37]) in direction i interpreted in the model as averaged *radii* of the ellipsoidal MTRs, and x, y, z are spatial coordinates.

Thus, assuming that the principal axes of the ellipsoid describing the average MTR align with the three primary wave propagation directions, the effective MTR diameter in the direction of wave propagation is $d_{MTR}^{i} = 2 \cdot a_{MTR}^{i}$.[16,27–29] These ultrasound-determined ellipsoidal diameters are compared to those derived from the autocorrelations calculated from the EBSD data in this work. Because the wavelengths typically used for ultrasound investigation of Ti are of the order of 0.6 mm, (at 10 MHz), the contributions of scattering from individual alpha crystallites (10 to 20 μm) are negligible to the ultrasound-measured correlation functions (*i.e.*, wavelength $\gg$ alpha grain size). This was

supported by estimates with the general scattering model[16,27,28] that includes crystallite scattering and its own crystallite autocorrelation function. Thus, the use of a single distribution to describe the ultrasonic scattering by MTRs is justified.

EBSD data collected for the purpose of characterizing MTRs often cover several mm^2 of area performed is at resolutions between 1 and 10 μm. The data therefore contain information on both short-range and long-range correlations affected by the primary alpha particles and MTRs, respectively. Thus, the EBSD-measured autocorrelation is a superposition of a correlation function describing the primary alpha particles and another describing the MTRs. Assuming that the each can be approximated by Poisson statistics, we can fit the autocorrelation for various r of interest using

$$\mathbf{S}_2^c(\mathbf{r}) \approx y_0 + C_{alpha} \exp\left(-\sqrt{\mathbf{r}^2/(a_{alpha}^{r})^2}\right) + C_{MTR} \exp\left(-\sqrt{\mathbf{r}^2/(a_{MTR}^{r})^2}\right)$$

[9]

where C_{alpha} and C_{MTR} are fitting constants, a_{alpha}^{r} and a_{MTR}^{r} are the *radii* of the primary alpha particles and MTR distributions, respectively, and y_0 is the value to which the autocorrelation decays (defined by macrotexture). Thus,

$a^{\mathbf{r}}_{\mathrm{MTR}}$ is measurable by ultrasound and EBSD and is thus used as the representative length scale of the microstructure to compare in this work. The assumption of Poisson statistics is at least partially justified by the Palm-Khintchine theorem[38,39] which states that in cases where a signal arises from a large number of independent sources which are not necessarily Poissonian themselves and which do not independently contribute significantly to overall signal, then the signal itself is Poissonian.

III. RESULTS AND DISCUSSION

A. *Microstructure and Texture*

The microstructure of the as-received bar, shown in Figure 3, consisted of a combination of spheroidized α and transformed β. The fraction of retained β phase was 1.3 ± 0.2 pct. The secondary α was not organized into well aligned colonies as would be expected if they were formed during cooling following the last stage of thermomechanical processing but instead were deformed during a subsequent lower temperature processing step. The nominal diameter of the primary α particles was ~20 μm as calculated by the equivalent diameter method. No attempt was made to directly quantify the size of the secondary α laths/colonies in this work, because this size was significantly smaller than the wavelength of the incident ultrasonic wave, and therefore they are not strong contributors to the overall scattering behavior.

The texture of the α and β phases, shown in Figure 4, consisted of weak partial fibers aligned with the bar axis. In texture analysis, the term partial fiber implies that a crystal direction is aligned with a particular direction in the sample reference frame and that all rotations about this direction are present. It is noteworthy that axial sample symmetry, consistent with the geometry of the bar and the deformation process used to manufacture it, was imposed when calculating the orientation distribution function from which the pole figures were derived. The α texture consisted of two weak partial fibers, namely $\langle 10\bar{1}0 \rangle$ and [0001], both with intensities of ~1.5 multiples of a random distribution (mrd). There were distributions of orientations about these main texture components extending ~30 deg and ~20 deg from the **z**-axis, respectively, and the intensity of the fiber decreased approximately linearly with increasing distance from **z**. The β phase texture consisted of a $\langle 110 \rangle$ partial fiber with an intensity of 1.6 mrd. Collectively, these data show that the overall texture of the material was essentially random despite the presence of severe microtexture as shown below.

B. *Microtexture*

1. *Linear intercept method*

Microtextured regions in the longitudinal and transverse sections through the bar are evident in the crystal orientation maps in Figures 5 and 6, respectively. These figures contain: (a) crystal orientation maps, (b) crystal orientation maps with manually traced MTR boundaries, and (c) binary images of MTR boundaries used for
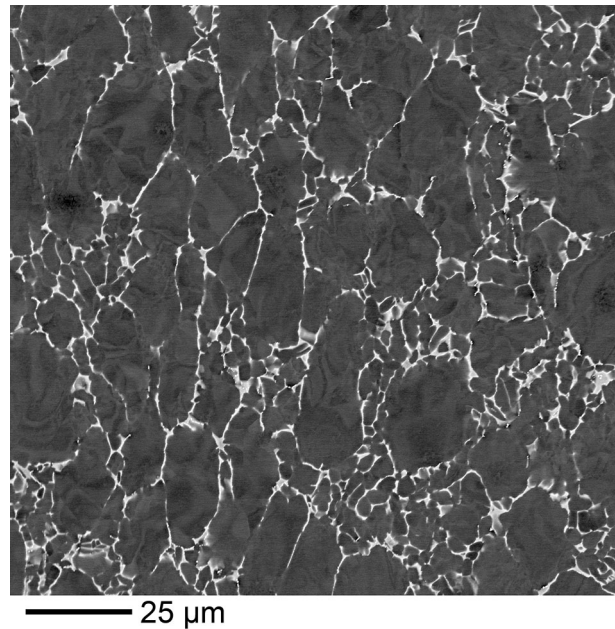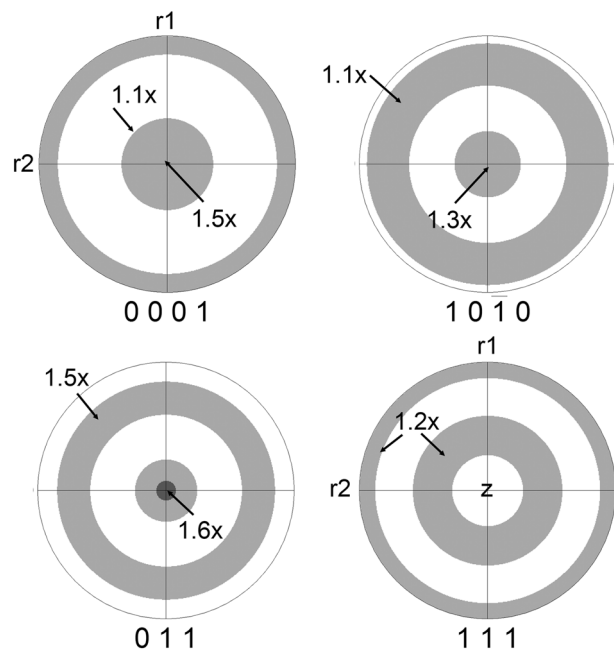

Fig. 3—Microstructure of the as-received bar in the **r1**–**z** plane.

Fig. 4—Texture of the α and β phases in the as-received bar (equal-area projections, axial sample symmetry).

calculating the linear intercepts. The average MTR size in the longitudinal direction from the manual tracing method, based on 38,162 intercepts, was 1.241 ± 1.49 mm, while the median value was 668 μm, and the maximum was 11.373 mm. Only longitudinal line intercept measurements were made on the manually identified boundaries of the longitudinal sample, because the inverse pole figure color representation was with respect to the **z**-axis of the bar. The large standard deviation relative to the mean reveals the significant scatter in MTR sizes measured by this method.
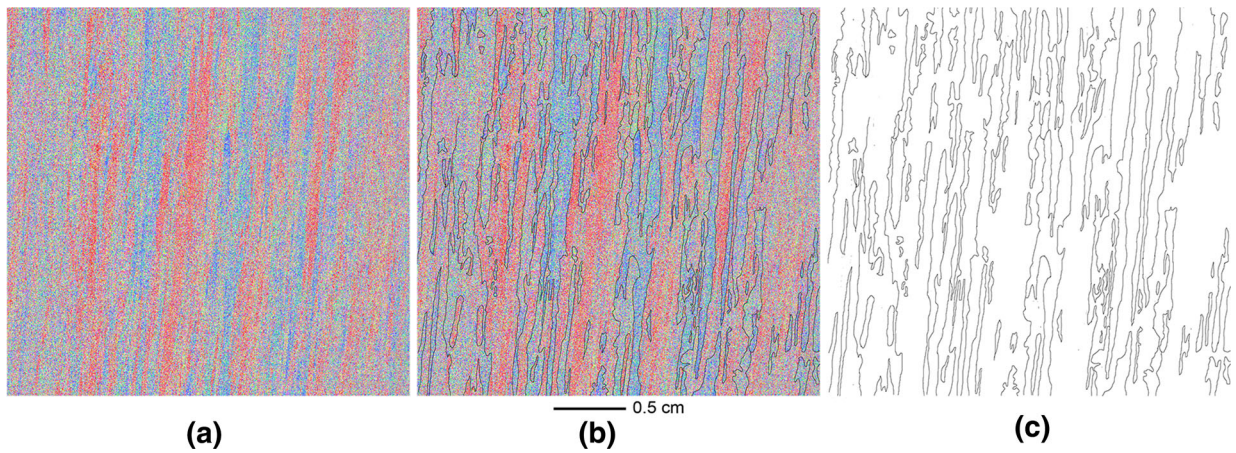
Fig. 5—EBSD data for the **z–r1** (vertical-horizontal) plane. (*a*) crystal orientation map, (*b*) crystal orientation map with manually segmented MTRs and (*c*) binary image used for line intercept calculations.
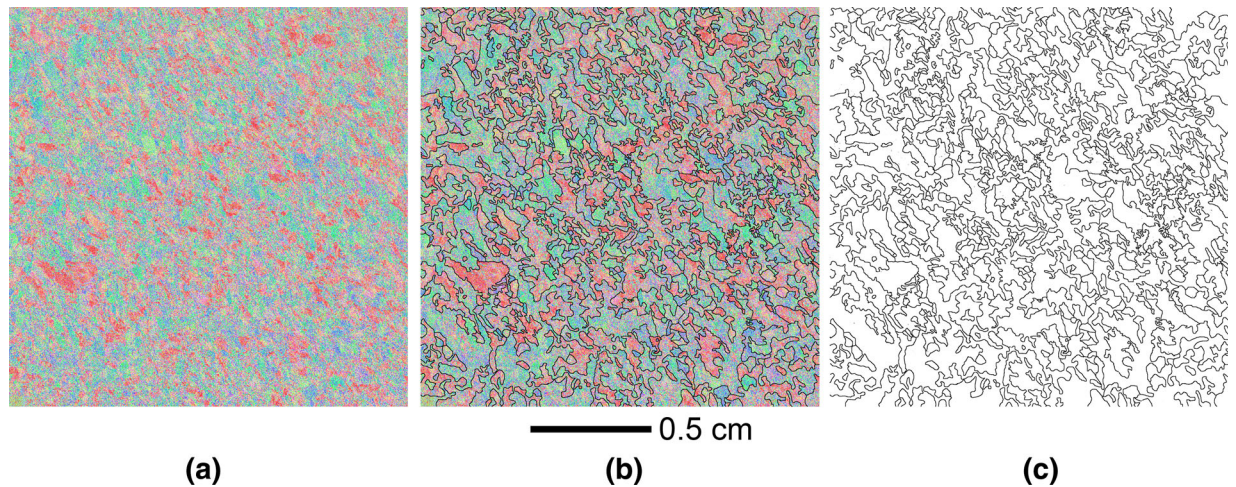

Fig. 6—EBSD data for the **r1–r2** (vertical-horizontal) plane. (*a*) crystal orientation map, (*b*) crystal orientation map with manually segmented MTRs and (*c*) binary image used for line intercept calculations.

MTR size in the transverse plane, Figure 6(c), was assessed using horizontal, vertical, and random line segments. All three were essentially equivalent measurements, since they were all made in radial directions in the axially symmetric bar. The binary image was constructed by tracing a radial direction crystal orientation map (horizontal axis in Figure 6) but was used to calculate all line intercepts. The line intercept statistics for the transverse plane are summarized in Table I. The similarities among the mean and median values for horizontal, vertical, and random line profiles indicate that the MTRs in the transverse sample orientation were essentially equiaxed. Figure 7 shows cumulative size distributions of the MTRs in the transverse and longitudinal sections. In the former case, the measurements include horizontal, vertical, and random lines (with respect to the images axes), while the latter only includes line profiles along the **z**-axis.

2. *Autocorrelation*

Representative autocorrelations of [0001] axes for a tolerance angle of 15 deg shown in Figure 8 reveal that contours of isoprobability are elliptical indicating that,

on average, MTRs can be approximated as ellipsoids. This alone is an important result as it justifies the use of this assumption in inverse ultrasonic scattering models.[16,27,28] The high aspect ratio of the MTRs in the longitudinal plane is obvious, as well as the slight inclination of the MTRs apparent in Figure 5. The contours are nearly equiaxed in the transverse plane, although some degree of preferential elongation approximately 30 deg to the vertical is evident. Autocorrelations like those shown in Figure 8 were calculated for various tolerance angles from which line profiles originating at the center and extending along vectors parallel to the principal sample axes are plotted for comparison in Figure 9. The data represent the probability of finding pixels separated by a given distance in which the angle between c-axes is less than the specified tolerance angle. No information regarding the state of microstructure along **r** can be extracted from these data; however, the shape of these curves is directly related to the microstructure. The autocorrelation functions initially decay strongly exponentially. Similar exponentially decaying autocorrelation functions have been previously reported

Table I.   MTR Statistics for Transverse Sample Orientation Measured by Linear Intercept

	Mean (SD) (μm)	Median (μm)	Max (μm)	Number of Intercepts
r1	357 (259)	279	2493	101,496
r2	370 (279)	286	3363	97,866
Random Lines	372 (333)	270	3262	88,874
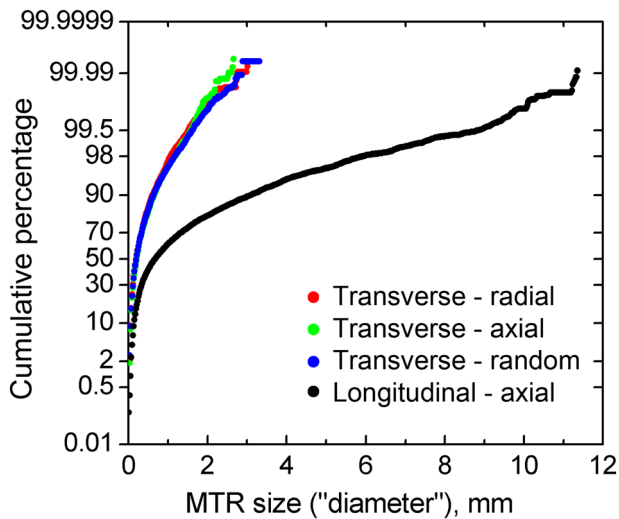
Fig. 7—Cumulative size distributions of MTR size in longitudinal and transverse samples.

Fig. 8—Autocorrelation of [0001] axes in the (*a*) longitudinal and (*b*) transverse planes based on a 15 deg discretization of sample space.

by Man *et al.*,[37] Gao *et al.*,[40] and Moreau *et al.*[41] In this case, we display the data on a logarithmic scale to emphasize the dual nature of the distribution. The first steep drop on each curve corresponds approximately to the primary alpha particles which were of the order of 20 μm in diameter. Correlations beyond the alpha particle size indicate there were neighboring constituents in the microstructure (either primary alpha or transformed beta) that had similar c-axis orientations. In this work, because the MTRs were the primary scatterer of the ultrasonic waves, we have made no attempt to separate the contributions of each, although there are techniques available to do so.[42] The fact that the smallest tolerance angles have near-zero long range correlations is not surprising given that the bar experienced significant alpha + beta working, and the crystal orientation maps (Figures 5 and 6) also show significant orientation gradients.

A comparison of $S_2^c(\mathbf{r})$ for $\mathbf{r}$ parallel to the sample **r1**, **r2**, and **z** axes provides insight into the effective aspect ratio of the MTRs as measured in the sample reference frame. Comparing probabilities for a given correlation length and tolerance angle in Figures 9(a) *vs* (b) and Figures 9(c) vs (d), for example, it is evident that the former are essentially indistinguishable from one another indicating the equiaxed morphology of the MTRs in the transverse section. The longitudinal sample exhibited MTRs highly elongated in the **z**-direction compared to the radial direction. A quantitative comparison is made by fitting each autocorrelation in Figure 9 (dashed curves) to Eq. [9]. The generally low residual of the fitted curves (the largest being a
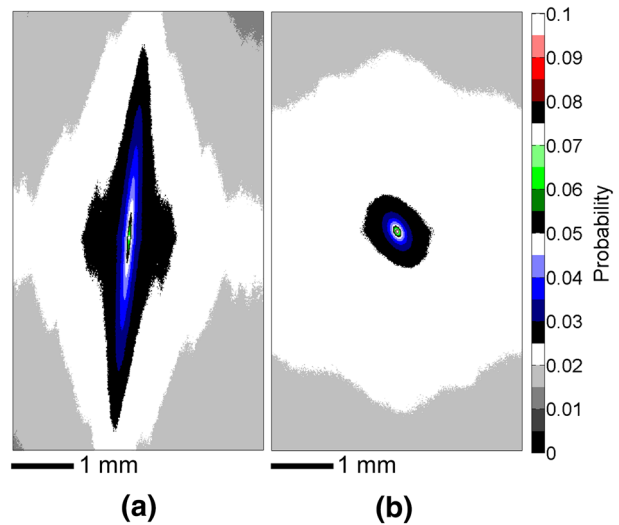
probability of 0.01 for a tolerance of 20 deg at a correlation length of 8 pixels, or 80 μm, and the fitted value of y_0 was of the order of 0.06) indicates that the experimental data are well described by Poisson statistics. Thus, we can invoke the relationship between the parameters in Poisson's geometrical autocorrelation function and the mean intercept length proven by Stanke[33] and Man *et al.*[37] The so-obtained MTR sizes for different **r** are summarized in Table II, and the corresponding aspect ratios are reported in Table III.

C. *Ultrasonic Measurement Results*

A variation in local attenuation was observed in all three directions of measurement. It was found that the manually measured attenuation at the center of each face was nearly equal to the averaged attenuation acquired in scanning mode. Since manual measurements are considered to be more accurate, the manually measured attenuation coefficient at the center of each face was selected as representative for the sample in each of the three orthogonal directions. The attenuation coefficients from each two opposite faces of the sample were averaged to represent α in that direction. The frequency-dependent attenuation coefficients in three orthogonal directions of the sample in Figure 10 show a significantly larger value in the axial direction in which the MTRs were elongated; also the attenuation coefficients in the two radial directions were not equal.

The time-domain backscattering signal in a single sample location and its frequency domain RMS are shown in Figure 11. A large difference in backscattering
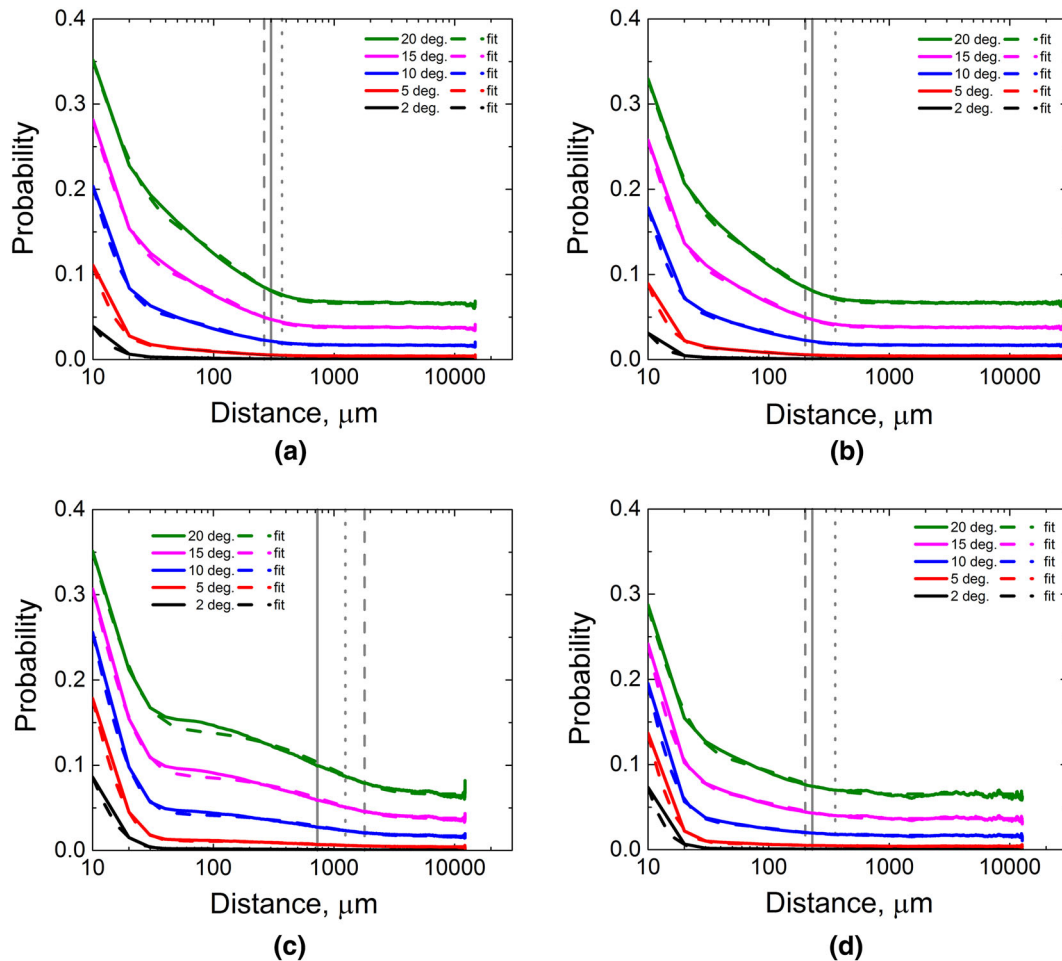
Fig. 9—Results from autocorrelation analysis for (*a*) transverse section, **r1** direction, (*b*) transverse section, **r2** direction (*c*) longitudinal section, billet **z**-axis direction and (*d*) longitudinal section, radial direction. Solid, long dashed and short dashed vertical lines represent the MTR sizes obtained from ultrasound, autocorrelation and mean linear intercept, respectively.

amplitude is observed in both the time and the frequency domains. In Figure 11(a), the time scale for the backscattering signal in the axial direction is shorter because of the small sample thickness in this direction. As one can see, the backscattering signal is much smaller in the axial direction (parallel to the MTR elongation direction). This is exactly opposite to the behavior of attenuation, which is the largest in this direction (Figure 10). As discussed below, this behavior is consistent with the theoretical model predictions. In addition, this inverse behavior of attenuation and backscattering relative to the elongation of the primary scatterer has been observed in previous experiments in other studies.[16,22,23]

Figure 12 shows spatial distributions of the backscattering RMS (a) and attenuation coefficient (b) obtained in scanning mode in the axial (*z*) direction. At a given transducer location, the average backscattering signal RMS over 5.5 mm of sample thickness was used to represent the pixel value in the image. One can see significant spatial variation of the ultrasonic parameters indicating the spatial heterogeneity of the MTRs in the sample. Spatial distributions in the

ultrasonic images show overall the similar opposite behavior (increase–decrease of attenuation *vs* RMS) in different sample locations as those discussed above for averages. For example, as seen in Figures 12 (a) and (b), in the upper region of the sample, attenuation has higher value, while backscattering has lower value relative to the nominal value.

D. *Analysis of Ultrasonic Measurements and Evaluation of MTR Size and Morphology from Ultrasonic Data*

1. *Theoretical background: ultrasonic backscattering and attenuation in microtextured Ti alloys*

Due to the stochastic nature of polycrystalline media, ultrasonic wave propagation in polycrystals is a complex wave phenomenon. It depends on the elastic properties of the material microstructure which is described by the elastic stiffness tensor c_{ijkl}. As the wave propagates, it scatters due to changes in crystallographic orientation of the grains in the wave propagation path. This change of crystallite orientation is described by small random variations $\delta c_{ijkl}(\mathbf{X})$ of the elastic stiffness tensor, *i.e.*, $c_{ijkl}(\mathbf{X}) = c_{ijkl}^0 + \delta c_{ijkl}(\mathbf{X})$, as functions of the spatial

Table II. Alpha Particle and MTR Sizes Obtained from Autocorrelation of [0001] Axes

Plane/Direction	Resolution (deg.)	y_0	$2*a_{alpha}$ (μm)	$2*a_{MTR}$ (μm)
Transverse **r1**	2	6.78e−4	8.60	217
	5	4.23e−3	9.84	231
	10	1.68e−2	12.44	247
	15	3.76e−2	15.6	262
	20	6.61e−2	19.32	276
Transverse **r2**	2	6.83e−4	7.76	182
	5	4.26e−3	8.98	186
	10	1.69e−2	11.24	196
	15	3.79e−2	13.90	206
	20	6.66e−2	16.88	216
Longitudinal **r1**	2	6.59e−4	7.60	252
	5	4.11e−3	9.78	326
	10	1.64e−2	11.16	279
	15	3.66e−2	11.76	261
	20	6.44e−2	12.08	259
Longitudinal **z**	2	6.87e−4	10.86	1661
	5	4.29e−3	12.46	1693
	10	1.70e−2	14.84	1740
	15	3.78e−2	17.06	1842
	20	6.63e−2	19.24	1945

Table III. MTR Aspect Ratios from EBSD

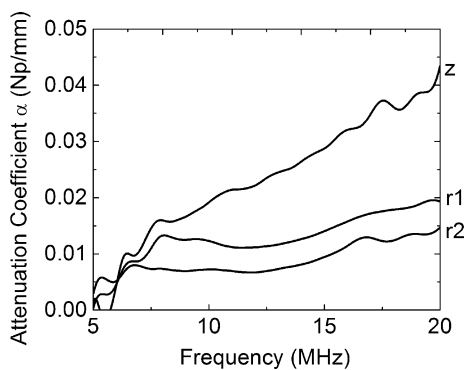| Resolution, deg:	Transverse **r1**/ Transverse **r2**	Longitudinal **z**/ Longitudinal **r1**	Longitudinal **z**/ Transverse **r1**	Longitudinal **z**/ Transverse **r2**
2	1.19	6.58	7.66	9.13
5	1.24	5.20	7.34	9.08
10	1.26	6.23	7.03	8.90
15	1.27	7.05	7.04	8.95
20	1.28	7.51	7.04	8.99

Fig. 10—Attenuation *vs* frequency response in three sample directions.

coordinate **X**; c_{ijkl}^0 is the macroscopic elastic tensor of the homogenized polycrystalline medium, and the spatial average of δc_{ijkl} is zero. As a random inhomogeneous medium, the material microstructure can be mathematically described by a hierarchy of n-point correlation functions. The two-point or pair correlation function (PCF) $\langle \delta c_{ijkl}(\mathbf{X}) \delta c_{\alpha\beta\gamma\delta}(\mathbf{X'}) \rangle$ for the elastic tensor fluctuations δc_{ijkl} is a probability density for having two different crystallographic orientations of grains specified by the points **X** and **X'** (brackets $\langle \ldots \rangle$ indicate spatial averaging). The two-point correlation function plays a central role in the theory of elastic wave propagation in polycrystals and the resulting model dependences of ultrasonic wave attenuation and backscattering on material characteristics and the frequency spectrum of the probing ultrasonic wave. Since the PCF depends on grain size and morphology, it has implications on scattering at grain boundaries, and it therefore appears naturally in ultrasonic scattering models.[24,27,28]

Closed form solutions for ultrasonic wave propagation and scattering applicable to near-α titanium alloys with microtexture have been obtained in the literature.[16,27,28] In this work, in order to compare ultrasonic and EBSD measurements, we will use simplified, approximate relations obtained from general theory for description of attenuation and backscattering coefficients. In this approximation, scattering from individual alpha crystallites is not considered, since scattering from the MTRs is dominant. Further, we will consider that the MTRs have a set of effective elastic properties which depends on the orientation distribution function (ODF) within individual MTRs, but averaged over all MTRs.[16]

Under these conditions and invoking the result from Figure 8 that MTRs can, on average, be described as general ellipsoids, the backscattering coefficient for longitudinal wave η is[27,28]:
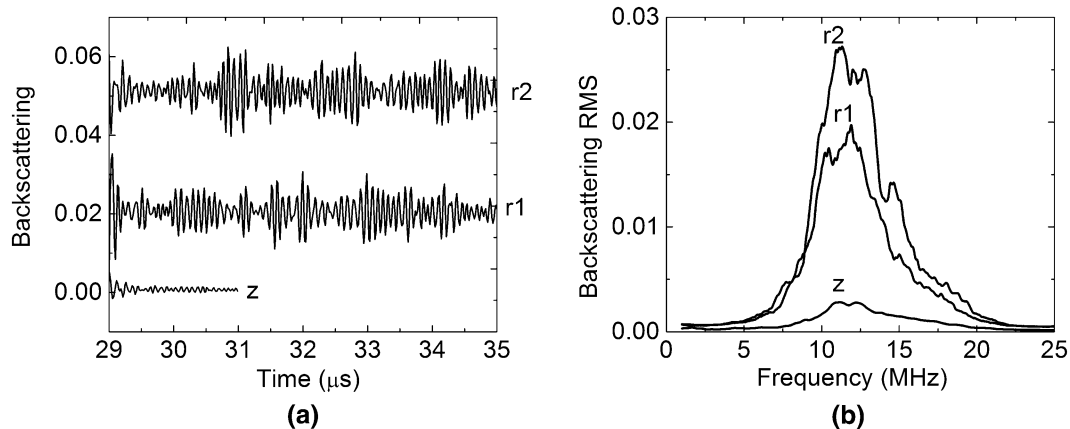
Fig. 11—(*a*) Time-domain backscattered signal and (*b*) backscattering RMS *vs* frequency in three sample directions. Note the significantly larger attenuation in the **z**-direction in Fig. 10 and the corresponding reduction in the backscattering amplitude in this direction.
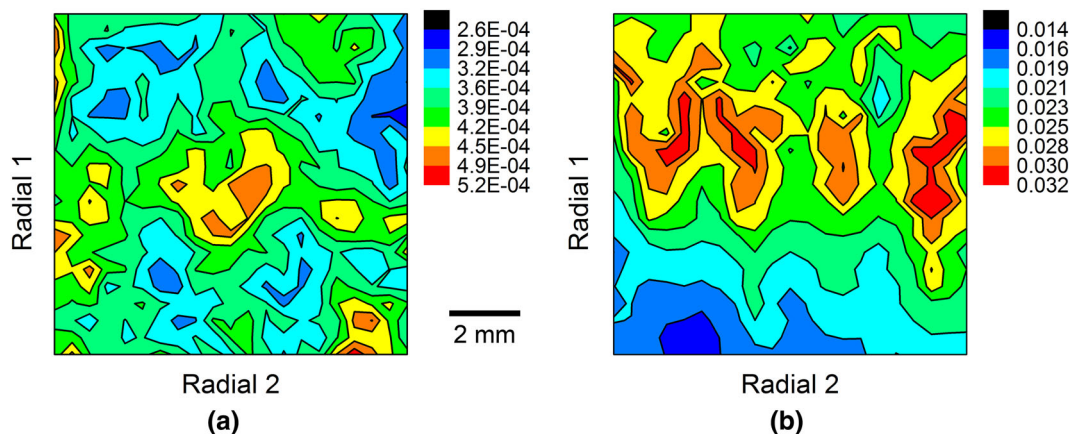

Fig. 12—Spatial distribution of (*a*) backscattering RMS (*b*) attenuation coefficient in the axial (*z*) direction obtained in scanning mode with a step size of 0.5 mm.

$$\eta = QVk_L^4 \left(\frac{1}{(1 + k_L^2 l_{\mathbf{r}}^2)^2} \right) \qquad [10]$$

where $V = 8\pi a_x a_y a_z$ is defined as the effective volume of the average MTR; $a_x = a_{MTR}^{\mathbf{r1}}$, $a_y = a_{MTR}^{\mathbf{r2}}$, and $a_z = a_{MTR}^{\mathbf{z}}$ are the main ellipsoidal radii. $k_L = 2\pi f/c_L$ is the wavenumber, f is frequency, c_L is longitudinal velocity in the medium, and $l_{\mathbf{r}}$ is the interaction length along the wave propagation direction **r** which is interpreted in Figure 13 as the distance from the wave front entrance into the ellipsoid to its exit. For wave propagation along the principal axes of the effective ellipsoid, the interaction length is exactly equal to the diameter of the average MTR in the wave propagation direction.

The nondimensional elastic (tensorial) factor Q in Eq. [10] is defined[28] as a normalized covariance for the MTR; it depends on the α crystallite ODF in the MTR.[16] The determination of the effective elastic properties of the MTRs and the parameter Q, which are related to the degree of misorientation of the crystallites within the MTR is described in Reference 16. For samples of the same composition, Q may vary from one sample to another due to thermomechanical

processing history, and thus, Q is unknown a priori. For a macroscopically isotropic sample, Q is independent of wave propagation direction.

The solution for the ultrasonic attenuation coefficient of a microtextured material is more complex and reduces to 2-D integrals[16,26] over the whole space, since attenuation is induced by scattering in all directions. The solution for MTR-induced attenuation can be significantly simplified in the stochastic region[26] where the wavelength of ultrasound λ is smaller than the average MTR size. In this regime, the attenuation coefficient α can be represented as

$$\alpha = Q \cdot 4\,\pi^2 k_L^2 a_{MTR}^{\mathbf{r}} \qquad [11]$$

where k_L is the wavenumber; $a_{MTR}^{\mathbf{r}}$ is the *radius* of the average MTR in the wave propagation direction **r**. As illustrated in Figure 13, $a_{MTR}^{\mathbf{r}}$ equals half of the ellipsoid dimension that is in the direction of wave propagation and is also approximately half of the interaction length, but the exact relationship depends on the inclination of the principal MTR axis with respect to the wave propagation direction. The elastic factor Q is the same as in Eq. [10]. As seen from Eqs. [10] and [11], the
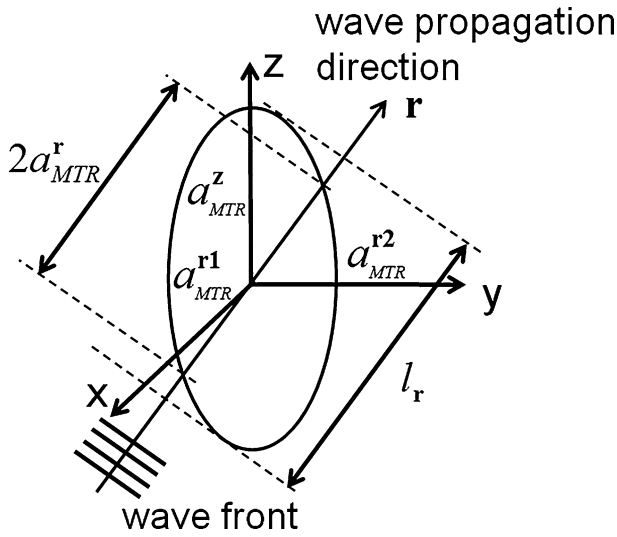
Fig. 13—Geometry of an idealized MTR modeled as a general ellipsoid. The ultrasonic wave propagates in an arbitrary direction **r** with wave vector **k** while l_r and r are interaction length and ellipsoidal radius in propagation direction, respectively.

backscattering coefficient is inversely proportional to the fourth power of the interaction length, while the attenuation is proportional to the ellipsoid radius, which essentially explains the opposite effects of MTR size in the direction of wave propagation on backscattering and attenuation coefficients. It is clearly seen from the experimental attenuation and backscattering data shown in Figures 10 and 11 that MTR size has opposite effects on backscattering and attenuation. In the axial propagation direction (the largest MTR size), the backscattering is smallest, while the attenuation is largest. The converse is true in the radial directions, where the backscattering is largest and attenuation is smallest. Such an opposite behavior of the experimental backscattering and attenuation coefficients on size is consistent with the model predictions.[16]

2. *Backscattering and attenuation coefficients ratios: MTR aspect ratio*

Since the parameter Q in Eqs. [10] and [11] is unknown, it is advantageous to use the ratio of backscattering coefficient obtained in different propagation directions of the sample. This methodology was developed[27,28] for the inverse determination of the average radii of the ellipsoidal MTRs from backscattering coefficient measurements in different propagation directions. In this method, the elastic factor Q is canceled thereby reducing the number of parameters to be determined. Also, in the backscattering ratio method,[28] the system parameters are excluded without deconvolution by the reference signal allowing one to increase the frequency bandwidth of the method. The same argument can be applied to the ratio of attenuation coefficients Eq. [11] in different propagation directions. Thus, for estimation of the MTR radii, we first analyze the ratio of these coefficients.

The RMS of the measured backscattering signal normalized by the transducer frequency response is

proportional to the square root of the backscattering coefficient $\sqrt{\eta(f)}$[17,18,43] obtained in our analysis. In the use of Eq. [10], we first observe that in the MHz frequency range with the MTR sizes studied in this work, the nondimensional wave number $k_L l_r \gg 1$, and the backscattering coefficient becomes

$$\sqrt{\eta(f)} = \frac{1}{l_r^2} \sqrt{Q \cdot V} \qquad [12]$$

Ratios of MTR sizes in propagation directions **ri** and **rj** are estimated as

$$\sqrt{\eta_i(f)}/\sqrt{\eta_j(f)} = l_{rj}^2 / l_{ri}^2 \qquad [13]$$

By taking ratios of backscattering RMS, Eq. [13], all proportional factors of Eq. [12] are canceled, and the ratio of the square roots of the RMS is simply the inverse ratio of interaction lengths l_i. Similarly for the attenuation ratios

$$\alpha_i(f)/\alpha_j(f) = a^{ri}/a^{rj} \qquad [14]$$

The attenuation coefficient ratio Eq. [14] provides the ratio of the MTR radii in the propagation directions. One should note that in this approximation, the ratios Eqs. [13, 14] are frequency independent.

The ratios of the experimental backscattering amplitudes RMS in different propagation directions *vs* frequency are shown in Figure 14(a) and the ratio of attenuation coefficients in Figure 14(b). From those figures and Eqs. [10] and [11], it can be seen that $l_z > l_{r1} > l_{r2}$, which is consistent with the EBSD measurements. To successfully use Eq. [13] to estimate the interaction length ratio from the experimental data in Figure 14(a), it is important to select the applicable frequency range. It is determined from Figures 10 and 11(b) that this is the mid frequency range (8-14 MHz) where the signal amplitude is sufficiently strong. The result for the backscattering RMS ratio and the attenuation coefficient ratio are shown by dashed lines in Figure 14 and also in Table IV.

3. *Attenuation-to-backscattering ratios: directional size of MTRs*

Due to the large size of the MTRs, many of which are comparable to or larger than the ultrasonic wavelength, the measured backscattering data are in the high frequency range $(k_L l_r \gg 1)$ of the ultrasonic backscattering coefficient[28] (*i.e.*, the flat range of the backscattering coefficient curves). In this high frequency range, the inversion of experimental directional backscattering ratios[27,28] for absolute MTR size determination is not stable, and only the MTR morphology (as was done in the previous section) can be determined. To estimate absolute MTR size in different propagation directions, we have employed the recently developed[29] attenuation-to-backscattering ratios method which is applicable in the frequency range and MTR sizes investigated here.

By combining Eqs. [11] and [12], we have

$$\sqrt{\frac{\alpha}{\eta}} = 8\pi k_L \frac{(l_\mathbf{r}/2)^2 \sqrt{a_{MTR}^\mathbf{r}}}{\sqrt{V}} \qquad [15]$$

where $l_\mathbf{r}$ is the interaction length, and $a_{MTR}^\mathbf{r}$ is ellipsoid radius in wave propagation direction $\mathbf{r}$. The square root of the ratio is used as it is related to the measured backscattering amplitude. It is advantageous to define a directionally dependent effective size parameter $R_{eff}^\mathbf{r}$,[29] which has dimensions of length

$$R_{eff}^\mathbf{r} = \frac{(l_\mathbf{r}/2)^2 \sqrt{a_{MTR}^\mathbf{r}}}{\sqrt{V/8\pi}} \qquad [16]$$

From Eq. [15], $R_{eff}^\mathbf{r}$ is directly represented through measurable parameters ultrasonically for various $\mathbf{r}$:

$$R_{eff}^\mathbf{r} = \frac{c_L}{4\pi\sqrt{2\pi}f} \sqrt{\frac{\alpha}{\eta}} \qquad [17]$$

where an averaged experimental velocity c_L = 6.3 mm/μs. The advantage of using the attenuation-to-backscattering coefficient ratio is that the elastic factor Q appearing in Eqs. [10] and [11] is canceled, and thus full knowledge of the single crystal elastic constants is not necessary to apply this method. For elucidation of the physical meaning of the effective size parameter $R_{eff}^\mathbf{r}$, it is useful to note that for equiaxed MTRs, $l_\mathbf{r} = 2 \cdot a_{MTR}^\mathbf{r} = d_{MTR}^\mathbf{r}$, and the effective size parameter equals the average MTR radius, $R_{eff}^\mathbf{r} = a_{MTR}^\mathbf{r}$. For ellipsoidal

MTRs in which the wave propagation is parallel to the principal axis of the MTR, the diameter in the propagation direction is equal to the interaction length, $l_\mathbf{r}$. In the axial direction, for example, $l_\mathbf{z} = 2 \cdot a_{MTR}^\mathbf{z}$. However, the effective parameter $R_{eff}^\mathbf{r}$ also depends on the MTR cross-section in the plane perpendicular to the wave propagation direction. For example,

$$R_{eff}^\mathbf{z} = (a^\mathbf{z})^2 / \sqrt{a^{\mathbf{r1}} \cdot a_{MTR}^{\mathbf{r2}}}, \qquad [18]$$

where $a_{MTR}^{\mathbf{r1}}$ and $a_{MTR}^{\mathbf{r2}}$ are the principal MTR radii in the plane orthogonal to $\mathbf{z}$. The dependences of the experimental $\sqrt{\alpha/\eta}$ ratios in the 9 to 14 MHz frequency range were used for the averaged MTR diameter determination. First, the effective size parameter $R_{eff}^\mathbf{r}$ was determined for $\mathbf{r} = \mathbf{r1}, \mathbf{r2}$, and $\mathbf{z}$ independently for each of the 3 directions from the $\sqrt{\alpha/\eta}$ ratios. For data analysis, the semi-axes of the average MTR were assumed to be aligned along the principal axes of data collection. In this case, $l_\mathbf{r} = 2 \cdot a_{MTR}^\mathbf{r}$, and $V = 8\pi \cdot a_{MTR}^{\mathbf{r1}} \cdot a_{MTR}^{\mathbf{r2}} \cdot a_{MTR}^\mathbf{z}$. Using the effective size parameters determined from Eq. [17] for all three directions, one obtains the system of Eqs. [18] for averaged MTR radii $a_{MTR}^{\mathbf{r1}}; a_{MTR}^{\mathbf{r2}}; a_{MTR}^\mathbf{z}$. These sizes are directly related to microstructure through Poisson's geometric autocorrelation function used in the inversion model and are therefore a measure of the degree of microtexture in the material. Figure 15 compares the attenuation-to-backscattering ratios: wavy solid lines are measured, and dashed lines are calculated using Eq. [15]; the ultrasonic-determined ellipsoid diameters
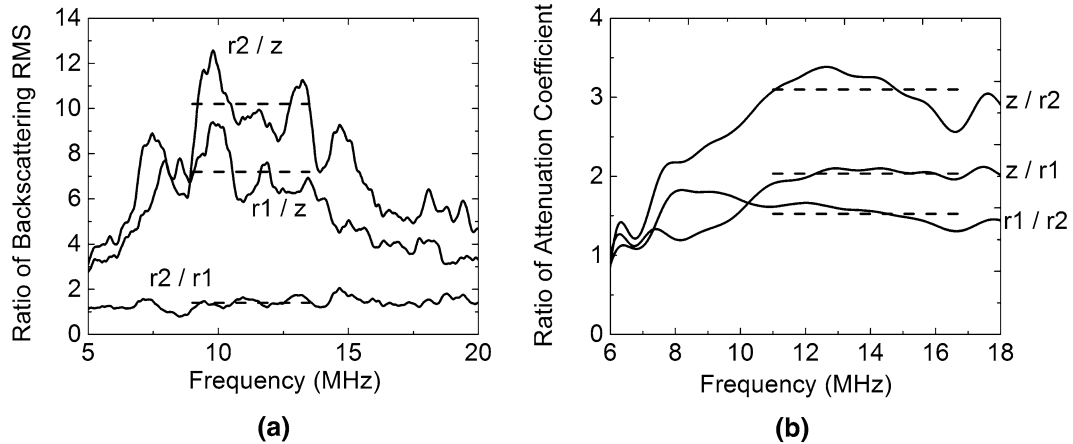

Fig. 14—Measured ratio (irregular solid lines) of backscattering RMS (a) and attenuation coefficients (b). Dashed lines are estimation of the ratios from Eqs. [13] and [14].

Table IV. MTR Aspect Ratios Obtained from Ultrasonic Measurements

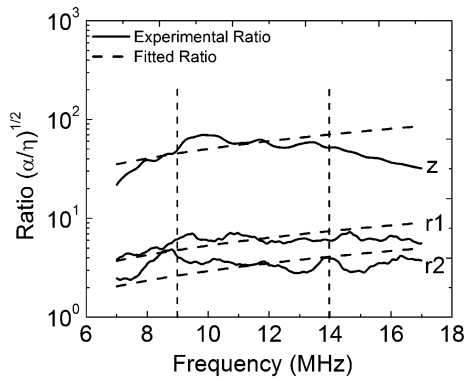| Sample Direction Ratio	Ultrasound		
	Backscatter Ratio $(\eta_\mathbf{i}/\eta_\mathbf{j})^{1/2}$	Attenuation Ratio $\alpha_\mathbf{i}/\alpha_\mathbf{j}$	Direct Fitting Att-BS Ratio
z/r1	2.7	2.0	2.4
z/r2	3.2	3.0	3.2
r1/r2	1.2	1.4	1.3

Fig. 15—Wavy solid lines are experimental attenuation-to-back-scattering ratios $\sqrt{\alpha/\eta}$; dashed lines are calculated by the approximate model Eq. [15] with the MTR size parameters from Table V.

reported above were used for the calculations. The results demonstrate the quality of the data analysis in the mid frequency range. The discrepancy at high frequency is mainly due to the bandwidth limit of the ultrasonic transducers and the resulting susceptibility to noise in this range of the signal deconvolution that was used for the ultrasonic data processing.

4. Determination of the effective elastic Q factor of the MTR from absolute backscattering amplitude coefficients

As discussed previously, both attenuation and backscattering coefficients depend on the nondimensional (normalized) elastic (tensorial) factor Q. In the present work, the averaged directional sizes of the MTRs were determined by considering directional attenuation-to-backscattering ratios which exclude Q from the inversion calculation. Nevertheless, the factor Q is an important quantity as it is a semiquantitative measure of the effective ODF of the MTRs in the volume of material over which the elastic wave interacted. Practically speaking, these local misorientations are one of the main contributors affecting the early stages of small, faceted crack growth in both dwell and cyclic fatigue loading.[2,44] This section briefly considers the determination of Q from EBSD and ultrasonic data.

While a typical ODF consists of many texture components representing the full distribution of orientations in a given sample, the ODF of an individual MTR can be expressed as the spread in orientation about a mean orientation. This is simply due to the fact that, as mentioned previously, an individual MTR is formed from an α colony which was well aligned and had negligible internal misorientations (assuming the β grains were annealed sufficiently long to permit some combination of recovery/recrystallization/grain growth). As the colony was deformed, localized lattice rotations and subgrain formation gave rise to misorientations between the α crystallites within the MTR leading to a spread in orientation about the main c-axis orientation of the MTR. Thus, the ODF can be modeled to the first order as an axisymmetric Gaussian distribution function of the form:[45]

$$F(\theta, \sigma) = F_0 \exp(\cos \theta / 2\sigma) \qquad [19]$$

where σ is the half width, called the microtexture parameter here, θ is the angular deviation from the primary texture component, and F_o is a normalization constant. In order to make a direct comparison of the ultrasonic and EBSD data, a method to obtain an average ODF for the MTRs was devised. First, the α crystallites were segmented from the raw EBSD data using a minimum misorientation criterion of 2 deg. Next, the average c-axis orientation of each grain was compared to its first nearest neighbors, and these were grouped together into an MTR if the c-axis misorientation was less than 15 deg (a tolerance angle of 25 deg was used on a second calculation to assess variability). Next, the average [0001] axis of each identified MTR was determined, and the angle between it and the c-axis of each α crystallite was calculated and recorded. These data were used to create distributions of frequency vs c-axis misorientation from the parent MTR average c-axis orientation. This served as an effective one-dimensional ODF averaged over all MTRs in the scanned area. These distributions were fitted with the model ODF Eq. [19] to obtain the effective σ. The experimentally determined MTR ODF and its corresponding approximation by a combination of Gaussian and uniform distributions are shown in Figure 16. The majority of the distribution is well approximated by the Gaussian except for angles below 1 deg which is covered by the uniform distribution. The disagreement here is negligible, since the reflection coefficient is small for slightly misoriented c-axes. This combined distribution was used for volumetric averaging to determine the effective properties of the MTRs and, eventually, parameter Q in Eqs. [10] through [12]. Increasing the MTR tolerance angle to 25 deg resulted in a six-fold increase in σ to ~0.03, but the magnitude of σ was still sufficiently small that the differences in the effective elastic parameters and Q would be negligible on ultrasonic scattering.

Following the approach of Yang et al.,[16] the elastic parameter Q was estimated from the α crystallite ODF of individual MTRs averaged over all of the sampled volume. Both weighted uniform and Gaussian distributions were used in the ultrasonic ODF model; it was found that the effect the uniform part on the Q is negligible. The measured absolute backscattering amplitude coefficient $\sqrt{\eta(f)}$ vs frequency f(MHz) is shown by irregular solid lines in Figure 17(a) in three orthogonal directions of the sample. Using the ultrasound-determined MTR sizes and $Q = 1.84 \times 10^{-5}$ for $\sigma = 0.005$, the absolute values of the amplitude backscattering coefficients in different propagation directions are calculated and shown by solid lines in Figure 17(a). The measured and calculated backscattering coefficients are in reasonable agreement, and the values are not sensitive to small changes in σ. The calculated backscattering amplitudes for $\sigma = 0.075$, a value obtained by ultrasound measurement for a forged Ti-6242 alloy, are shown in Figure 17(b) for the sake of comparison. One can observe clearly discrepancy between the

experimental values and those calculated for $\sigma = 0.075$ showing the importance of using an accurate σ. It has thus been demonstrated that variations in the internal misorientations in the MTRs (the "MTR ODF") can be determined by the ultrasonic measurements and that this value can also be approximated by EBSD.

One should note that the effective elastic parameter Q, characterizing an ultrasonic scattering strength by the MTRs, increases with σ decrease. However, when σ is small,[16] Q is weakly affected by σ, and therefore, an accurate inverse determination of σ at these values is not practical. With σ increase, Q changes more rapidly on σ, and the inverse determination of σ is more accurate. In previous work, a larger microtexture parameter σ (and smaller Q) was obtained by ultrasonic measurements for forged Ti-6242[16] (and elastic factor $Q = 7.47 \times 10^{-6}$). The microtexture of the forged materials was described in Reference 20. Larger σ is physically caused by an increase in the degree of crystallite misorientation within

MTRs. This can be due caused by forging or by post forge heat treatment which is intended to reduce the volume fraction of primary alpha followed by sufficiently rapid cooling to decompose the β phase to α lamellae thereby insulating the similarly oriented primary α particles.

IV. FURTHER DISCUSSION

The MTR sizes determined from EBSD and ultrasound, and the corresponding aspect ratios are reported in Tables V and VI. While the fitted alpha grain sizes increase monotonically with tolerance angle (Table III), the MTR size is less sensitive to this parameter. The values reported for the autocorrelation method in Table V are an average of the two values fitted at 10 deg and 15 deg tolerance angles. This choice is related to the increased uncertainty in the fitted y_0 and a_{MTR} at large and small tolerance angles, respectively, and the need to characterize larger regions for convergence of the autocorrelation of the former. The correlation function approaches y_0 rapidly at small tolerance angles, *viz.* 2 deg and 5 deg, leading to increased uncertainty in the fitted values of a_{MTR}. On the other hand, the function converges to y_0 slowly at large tolerance angles thereby requiring very large areas to be scanned which may permit other factors to confound the results. For example, because the features are so large, they may span locations which experienced different thermomechanical histories (the most important of which are total strain and its path), meaning that the mean MTR sizes/shapes may vary too greatly for description by Poisson statistics. Thus, the characterization area for EBSD and the volume of material interrogated in a particular gating of ultrasound for FFT, and inversion should be considered carefully with an appropriate process model. This is especially true for forgings with complex straining paths that cause wide variations in MTR size and in which the orientation of the MTRs is strongly influenced by the metal flow characteristics.
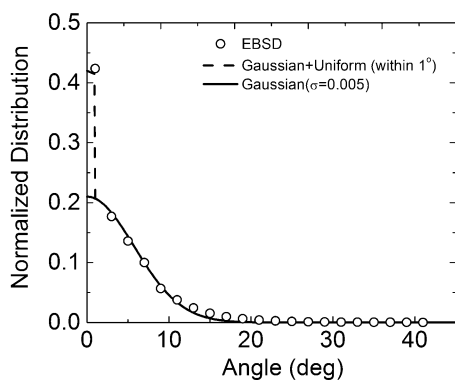

Fig. 16—The MTR ODF obtained from the EBSD images; the ordinate is the number of counts of a certain misorientation angle normalized by the total number of counts. The MTR ODF used in the ultrasonic model is approximated by a Gaussian function plus a uniform distribution within 1 deg; it normalized to match the EBSD data. Elastic parameters Q calculated for Gaussian distributions with and without addition of uniform distribution are equal within three digits ($Q = 1.84 \times 10^{-5}$).
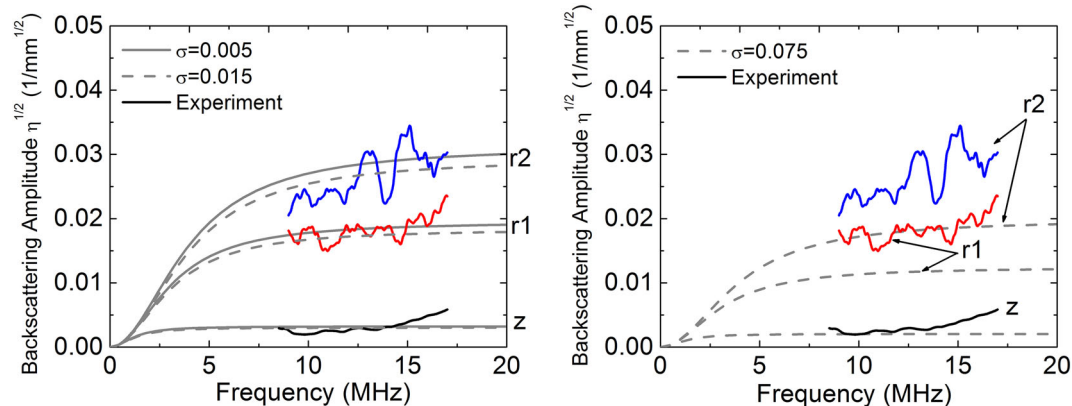

Fig. 17—Measured (irregular solid lines) and theoretical (solid and dashed gray lines) amplitude backscattering coefficients in different sample directions. The ultrasonic-determined MTR sizes used for theoretical curves are from Table V. (*a*) Backscattering coefficient calculated using elastic factor $Q = 1.84 \times 10^{-5}$ with microtexture parameter $\sigma = 0.005$ (solid gray lines) and $Q = 1.63 \times 10^{-5}$ with $\sigma = 0.015$ (dashed gray lines); (*b*) backscattering coefficient calculated for elastic factor $Q = 7.47 \times 10^{-6}$ with microtexture parameter $\sigma = 0.075$ that was used in Ref. [16]. Comparison with the experimental data indicates on much better agreement for the case in frame (a).

Table V. Comparison of Effective MTR Size obtained by Various Methods

Sample Direction	Effective MTR Dimensions (μm)			
	Mean*	Median*	EBSD**	Ultrasound†
r1	370	279	263	300
r2	357	286	201	230
z	1241	668	1791	730

*Obtained from manual segmentation and linear intercept.
**Average value of $2 \times a_{MTR}$ for 10 deg and 15 deg tolerance angles.
†Obtained by attenuation-to-backscattering ratio inversion method.

Table VI. Comparison of Effective MTR Aspect Ratios obtained by Various Methods

Sample Direction	Effective MTR Aspect Ratios			
	Mean	Median	EBSD	Ultrasound
z/r1	3.4	2.4	6.8	2.4
z/r2	3.5	2.4	8.9	3.2
r1/r2	1.0	1.0	1.3	1.3

It is evident that the MTR sizes obtained by manual segmentation and mean linear intercept are systematically larger than those obtained by autocorrelation. It is significant, however, that the mean sizes and all values in Table V are significantly smaller than the millimeter-scale dimensions that a typical researcher might assign to the MTRs by inspection of Figures 5 and 6. This is because the eyes are naturally drawn to the largest features in the dataset, which generally do not reflect the area (EBSD) or volume (ultrasound) averaged dimensions of the MTRs in the sample. This leads naturally for one to question why the characterization is being performed in the first place. If it is for the purpose of relation to mechanical properties, the mean MTR sizes may be acceptable to successfully "rank" the normal fatigue susceptibility of a batch of material relative to others through the use of a model.[46] This assumes that several other factors that influence fatigue behavior like primary alpha size are known from experiment or modeling. Dwell fatigue properties, on the other hand, are significantly more sensitive to the upper tail of the MTR size distribution and thus the mean values may be considerably less accurate for life prediction.

The values obtained by autocorrelation and ultrasound in Table V are in relatively good agreement in the radial directions, differing by a distance of less than 4 pixels in the EBSD scan (<40 μm). This difference of ~12 pct can be rationalized by the vastly different volumes of material interrogated with ultrasound compared to EBSD. In comparison, the agreement between the ultrasound and autocorrelation measurements in the axial direction is poorer with the mean sizes differing by a factor of 2.45. The reason for the discrepancy may be related to the lack of appropriate sampling statistics in the axial direction for ultrasound, since the first 5.7 mm from the front surface and 0.79 mm next to the back surface of the sample are not used in analysis due to very strong front and back reflections that mask backscattering signal (approximately 5.5 mm in the axial direction

was utilized for measurement). The correlation function for c-axes in the **z**-direction, Figure 9(c), did not converge to Eq. [9] within the distance traveled by the incident wave used for inversion. That is to say, there was no ultrasonic volume element in which the microstructure was sufficiently homogeneous to produce a characteristic signal. Thus, the MTR size in the axial direction determined by ultrasound is less reliable than that obtained by EBSD. Analysis of a sample in which the axial dimension is many times larger than the elongated MTR dimension is underway and is the subject of a future manuscript. Future work should also focus on samples with a tighter distribution of MTR sizes, e.g., smaller diameter bar[47] or rolled materials.

A unique aspect of the present work was that both destructive and nondestructive methods have been applied to quantify microtexture in near-alpha Ti billet. The two techniques are complementary, and both methods have their merits in terms of cost and speed of data acquisition, expense to purchase and maintain the equipment, and the area (or volume) of material interrogated. Ultrasound would be the preferred method from a practical perspective because it is routinely performed on critical aerospace components, and it is entirely nondestructive. The backscattering method is promising in this regard, because, in contrast to attenuation, it does not require flat, parallel surfaces to measure.

Figure 18 compares the experimentally measured and theoretically calculated directional ratios[27,28] of the backscattering amplitude RMS using selected MTR sizes reported in Table V. These data show the interrelation between the theoretical model and the destructive experimental characterization effort and also provide insight into the range of MTR sizes which still provide a reasonable agreement with the experimentally measured ultrasound data (in general, both MTR and crystallite scattering is accounted for in the model). Figures 18(a) and (b) show the comparison for the linear intercept measurements, while Figure 18(c) is based on
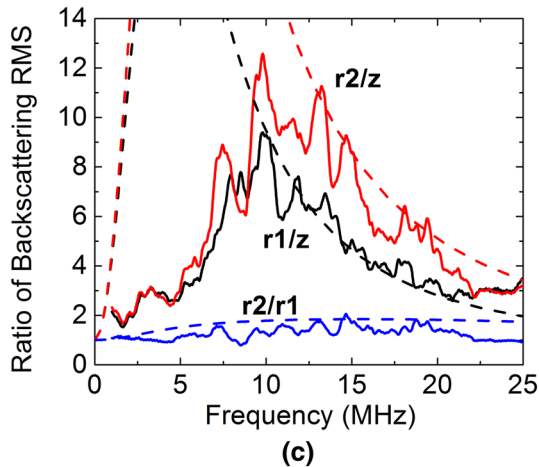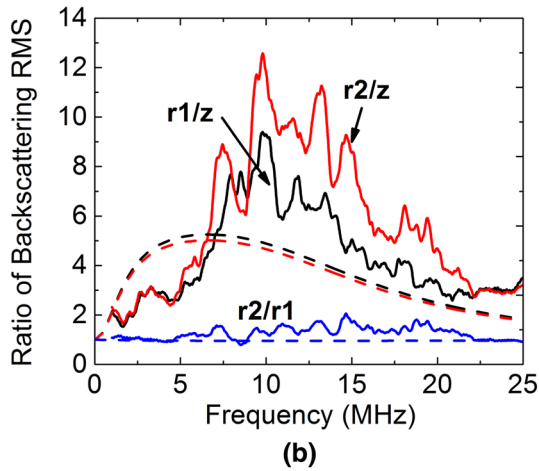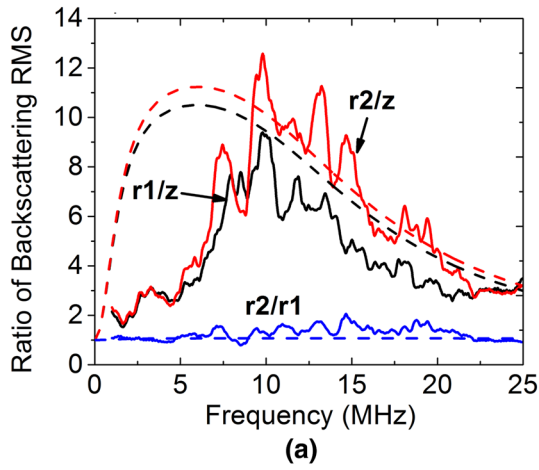
Fig. 18—Measured (irregular solid curves) and calculated (dashed lines) directional RMS of ultrasonic backscattering amplitudes. The effective MTR sizes used for calculations are from Table V: (*a*) mean linear intercept, (*b*) median linear intercept and (*c*) autocorrelation function.
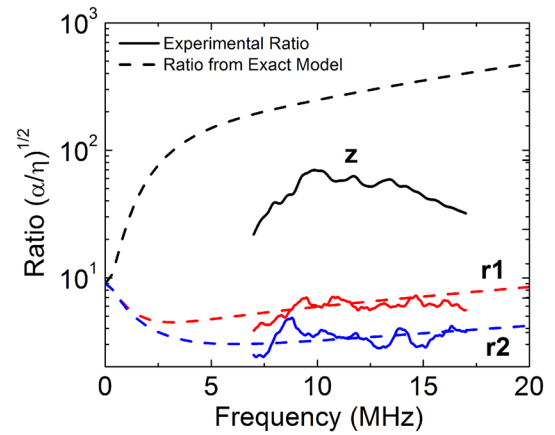
Fig. 19—Attenuation-to-backscattering ratios. Dashed curves are calculated with the radial MTR sizes (d_{MTR}^{r1} = 0.28 mm and d_{MTR}^{r2} = 0.20 mm) determined by the model fit; the MTR size in the axial direction, 1.791 mm, is assumed to be known from the EBSD measurements. Irregular solid curves are experiment.

discrepancy is observed at low frequencies mainly due to the effect of very low backscattering in the elongation (axial) direction **z** of the MTRs (experimental signal bandwidth is not sufficient). Motivated by the findings that the discrepancy is mainly due to the uncertainty in ultrasound-determined MTR size in the axial direction, we have fixed the MTR size in this direction to be equal to that obtained from EBSD (1.791 mm), and used the model to obtain the corresponding MTRs sizes from the ultrasonic data in **r1**, **r2** directions; they were found to be 0.28 and 0.20 mm, respectively. The comparison of the calculated and experimental results for the attenuation-to-backscattering ratios is shown in Figure 19. For the **r1**, **r2** directions, the agreement is excellent with the EBSD autocorrelation (Table V). Obviously a large discrepancy is observed in **z** (axial direction). As discussed above, this can be partially attributed to the size of the "ultrasonic scattering volume" in the axial sample direction which was only approximately three times the effective MTR size.

V. CONCLUSIONS

This work has shown a clear relation between ultrasonic attenuation and backscattering response and the morphology and size of MTRs in near-α titanium bar. EBSD was used to quantify the character of the MTRs using manual segmentation and autocorrelation of c-axes. The MTR sizes obtained in this way were compared to volume-averaged MTR measurements based on recently developed theoretical models for attenuation and backscattering response. The fundamental basis for this comparison is the use of a common autocorrelation function in both methods to characterize the MTRs. The following conclusions were reached:

1. Autocorrelation functions are an effective method to quantify the spatial arrangement of c-axes in a microstructure. These functions can be used to assess the alpha particle size as well as the presence of

the fit of the autocorrelation (Table II). The data show reasonable agreement between the measured and calculated backscattering coefficients for frequencies above 10 MHz (most of the frequency spectrum available in the experiment). The agreement for the median linear intercept sizes is not as good. However, significant

long-range correlations, *i.e.*, microtexture. The autocorrelation does not explicitly capture the attributes (average c-axis alignment) of individual MTRs (*i.e.*, there is no feature extraction). Thus, there remains a need for additional algorithm development to fully quantify them.

2. It is possible to use nondestructive techniques to quantitatively assess the aspect ratio of MTRs in titanium bar and obtain the volume-averaged size in each direction.

3. The MTR sizes obtained by destructive and nondestructive measurements were in good agreement in the radial directions in the billet, while the axial direction was off by a factor of ~2.45. Inspection of the autocorrelation function in the axial direction revealed that it had not converged over the distance traveled by the ultrasound in this direction. Thus, a stable, representative signal was not established resulting in increased uncertainty in the ultrasound inversion. Due to the extremely heterogeneous microstructure in the present billet material, future investigations should focus on more direct comparisons, if possible, including the incorporation of serial sectioning experiments.

4. Because the ultrasound energy is sampling both microtextured and "randomized" regions of material as it propagates through the volume of material, and these correlations (or lack of) are equally weighted with the long-range MTR correlations, the ultrasonic inversion methods return systematically smaller sizes than seem evident in the crystal orientation maps upon quick inspection. However, both the autocorrelation and manual segmentation methods resulted in mean sizes much less than this value as well.

REFERENCES

1. K. Le Biavant, S. Pommier, and C. Prioul: *Fatigue Fract. Eng. Mater. Struct.*, 2002, vol. 25, pp. 527–45.
2. A.P. Woodfield, M.D. Gorman, R.R. Corderman, J.A. Sutliff, and B. Yamrom: in *Titanium'95: Science and Technology*, P.A. Blenkinsop, W.J. Evans and H. Flower, eds., Institute of Materials, London, England, 1996, pp. 1116–23.
3. A.P. Woodfield, M.D. Gorman, J.A. Sutliff, and R.R. Corderman: in *Proceedings of an International Symposium on Fatigue Behavior of Titanium Alloys*, TMS, Warrendale, PA, 1999, pp. 111–18.
4. V. Sinha, M.J. Mills, J.C. Williams, and J.E. Spowart: *Metall. Mater. Trans. A*, 2006, vol. 37A, pp. 1507–18.
5. A.L. Pilchak and J.C. Williams: *Metall. Mater. Trans. A*, 2011, vol. 42A, pp. 1000–27.
6. A.L. Pilchak, K. Nakase, I. Inagaki, Y. Shirai, A.H. Rosenberger, and J.C. Williams: in *Proceedings of the 12th International Conference on Titanium*, L. Zhou, H. Chang, Y. Lu and D. Xu, eds., The Nonferrous Metals Society of China, 2012, pp. 1006–10.
7. P. Ari-Gur and S.L. Semiatin: *Mater. Sci. Eng. A*, 1998, vol. 257, pp. 118–27.
8. T.R. Bieler and S.L. Semiatin: *Int. J. Plasticity*, 2002, vol. 18, pp. 1165–89.
9. A.L. Pilchak and J.C. Williams: *Metall. Mater. Trans. A*, 2011, vol. 42A, pp. 773–94.
10. N. Stefansson, S.L. Semiatin, and D. Eylon: *Metall. Mater. Trans. A*, 2002, vol. 33A, pp. 3527–34.
11. N. Stefansson and S.L. Semiatin: *Metall. Mater. Trans. A*, 2003, vol. 34A, pp. 691–98.
12. A.A. Salem, M.G. Glavicic, and S.L. Semiatin: *Mater. Sci. Eng. A*, 2008, vol. 496, pp. 169–76.
13. N. Gey, M. Humbert, M.J. Philippe, and Y. Combres: *Mater. Sci. Eng. A*, 1996, vol. 219, pp. 80–88.
14. N. Gey, M. Humbert, M.J. Philippe, and Y. Combres: *Mater. Sci. Eng. A*, 1997, vol. 230, pp. 68–74.
15. M.F.X. Gigliotti, B.P. Bewlay, J.B. Deaton, R.S. Gilmore, and G.A. Salishchev: *Metall. Mater. Trans. A*, 2000, vol. 31A, pp. 2119–25.
16. L. Yang, J. Li, O.I. Lobkis, and S.I. Rokhlin: *J. Nondestruct. Eval.*, 2012, vol. 31, pp. 270–83.
17. R.B. Thompson, F.J. Margetan, P. Haldipur, L. Yu, A. Li, P. Panetta, and H. Wasan: *Wave Motion*, 2008, vol. 45, pp. 655–74.
18. R.B. Thompson and F.J. Margetan: *Wave Motion*, 2002, vol. 36, pp. 347–65.
19. B. Ginty, P. Hallam, C. Hammond, G. Jackson, and C. Robb: in *Titanium'80: Science and Technology*, H. Kimura and O. Izumi, eds., Kyoto, TMS-AIME, Warrendale, PA, pp. 2095–2103.
20. A. Bhattacharjee, A.L. Pilchak, O.I. Lobkis, J.W. Foltz, S.I. Rokhlin, and J.C. Williams: *Metall. Mater. Trans. A*, 2011, vol. 42A, pp. 2358–72.
21. Y.K. Han and R.B. Thompson: *Metall. Mater. Trans. A*, 1997, vol. 28A, pp. 91–104.
22. P.D. Panetta, R.B. Thompson, and F.J. Margetan: in *Review of Progress in Quantitative Nondestructive Evaluation*, 17, D.O. Thompson and D.E. Chimenti, eds., Plenum Press, New York, NY, 1998, pp. 89–96.
23. M.P. Blodgett and D. Eylon: *J. Nondestruct. Eval.*, 2001, vol. 20 (1), pp. 1–16.
24. L. Yang, O.I. Lobkis, and S.I. Rokhlin: *Ultrasonics*, 2011, vol. 51, pp. 303–09.
25. M. Humbert, A. Moreau, E. Uta, N. Gey, P. Bocher, and C. Bescond: *Acta Mater.*, 2009, vol. 57, pp. 708–14.
26. L. Yang, O.I. Lobkis, and S.I. Rokhlin: *Wave Motion*, 2012, vol. 49, pp. 544–60.
27. O.I. Lobkis and S.I. Rokhlin: *Appl. Phys. Lett.*, 2010, vol. 96, article 161905, pp. 1–3.
28. O.I. Lobkis, L. Yang, J. Li, and S.I. Rokhlin: *Ultrasonics*, 2012, vol. 52, pp. 694–705.
29. J. Li, O.I. Lobkis, L. Yang, and S.I. Rokhlin: in *Review of Progress in Quantitative Nondestructive Evaluation*, 31, D.O. Thompson, and D.E. Chimenti, eds., American Institute of Physics, New York, 2012, pp. 1397–404.
30. A.R. Shively, P.A. Shade, A.L. Pilchak, J.S. Tiley, and R. Kerns: *J. Microsc.*, 2011, vol. 244, pp. 181–86.
31. A.L. Pilchak, A.R. Shively, J.S. Tiley, and D.L. Ballard: *J. Microsc.*, 2011, vol. 244, pp. 38–44.
32. F.E. Stanke and G.S. Kino: *J. Acoust. Soc. Am.*, 1984, vol. 75, pp. 665–81.
33. F.E. Stanke: *J. Acoust. Soc. Am.*, 1986, vol. 80, pp. 1479–85.
34. R.L. Weaver: *J. Mech. Phys. Solids*, 1990, vol. 38 (1), pp. 55–86.
35. D. Rosca: *Astron. Astrophys.*, 2010, vol. 520 (A63), pp. 1–4.
36. J.G. Berryman: *J. Math. Phys.*, 1987, vol. 28, pp. 244–45.
37. C.-S. Man, R. Paroni, Y. Xiang, and E.A. Kenik: *J. Comput. Appl. Math.*, 2006, vol. 190, pp. 200–10.

38. E. Cinlar: in *Stochastic Point Processes: Statistical Analysis, Theory, and Applications*, P.A.W. Lewis ed., Wiley Interscience, New York, 1972, pp. 549–606.
39. S.G. Henderson: in *Proceedings of 2005 Winter Simulation Conference*, M.E. Kuhl, N.M. Steiger, F.B. Armstrong, and J.A. Joines, eds., 2005, pp. 120–29.
40. X. Gao, C.P. Przybyla, and B.L. Adams: *Metall. Mater. Trans. A*, 2006, vol. 37A, pp. 2379–87.
41. A. Moreau, L. Toubal, P. Bocher, M. Humbert, E. Uta, and N. Gey: *Mater. Charact.*, 2013, vol. 75, pp. 115–28.
42. A.A. Salem, M.G. Glavicic, and S.L. Semiatin: *Mater. Sci. Eng. A*, 2008, vol. 494, pp. 350–59.
43. F.J. Margetan, R.B. Thompson, and I. Yalda-Mooshabad: *J. Nondestruct. Eval.*, 1994, vol. 13 (3), pp. 111–36.
44. A.L. Pilchak: *Scripta Mater.*, 2013, vol. 68 (5), pp. 277–80.
45. J.H. Cho, A.D. Rollett, and K.H. Oh: *Metall. Mater. Trans. A*, 2004, vol. 35A, pp. 1075–86.
46. A.L. Pilchak: *Scripta Mater.*, 2014, vol. 74, pp. 68–71.
47. A.L. Pilchak, C.J. Szczepanski, J.A. Shaffer, A.A. Salem, and S.L. Semiatin: *Metall. Mater. Trans. A*, 2013, vol. 44A, pp. 4881–90.